Local structural effects of Eu3+ incorporation into xenotime-type solid solutions with different host cations

Xiao, B.; Lösch, H.; Huittinen, N.; Schmidt, M.;

Originally published:

July 2018

Chemistry - A European Journal 24(2018)50, 13368-13377

DOI: https://doi.org/10.1002/chem.201802841

Local structural effects of Eu^{3+} incorporation into xenotime-type solid solutions with different host cations

Bin Xiao[a], Henry Lösch[a], Nina Huittinen[a], and Moritz Schmidt*[a]

Abstract: In this study, the effect of host cations on the local structure around the dopant site of materials from the xenotime family is systematically studied on the molecular level. A series of six Eu^{3+}-doped xenotime-type single crystals (Tb, Y, Ho, Er Yb, and $LuPO_4$) have been grown and spectroscopically analyzed using polarization−dependent laser−induced luminescence spectroscopy (p−TRLFS). Our results demonstrate that the structural disorder changes in a non-linear manner with a structural break between Yb^{3+} and Lu^{3+}. Despite adopting identical crystal structures, the solid solutions of these materials vary significantly, and differ from monazite solid solutions. Similar Eu^{3+} incorporation behavior with a strongly distorted dopant site is found for the early members of the xenotime family, while $LuPO_4$ with the largest host vs. dopant radii mismatch is anomalous in that it contains the most symmetrical lattice site. This goes along with a significantly stronger crystal field, indicating a shorter Eu – O bond distance, as well as a strong vibronic coupling to external translational lattice vibrations. The p−TRLFS analysis confirms the breakdown of the crystallographic site symmetry from D_{2d} to C_1 in YPO_4, whereas a small distortion of the crystallographic site in $LuPO_4$ results in an S_4 point symmetry for the Eu^{3+} cation. The lattice with the smallest cation host site is no longer sufficiently flexible to make room for Eu^{3+} and instead "forces" the guest ion to occupy a less distorted Lu^{3+} site.

Introduction

Rare-earth orthophosphates $LnPO_4$ (Ln = La - Lu) with xenotime and monazite structures continue to attract the attention of chemists, mineralogists, and material scientists by virtue of their wide range of applications that include proton conductors[1], phosphors[2], catalysts[3] and medical imaging[4]. Phosphates which incorporate small cations in the second half of the rare-earth transition series from $TbPO_4$ to $LuPO_4$ (including YPO_4)[5] adopt a tetragonal xenotime-type structure (space group $I4_1/a$), while the larger rare-earth ions, from $LaPO_4$ to $GdPO_4$, are structural analogs of monoclinic monazite (space group $P2_1/n$).[6] Close to the xenotime-monazite boundary, orthorhombic solid solutions with anhydrite-like structures ($CaSO_4$) could be stabilized with mixed compositions, i.e. (e.g. $Gd_{0.4}Dy_{0.6}PO_4$[7] and $(Sm,Tb)PO_4$[8]). Apart from that, in aqueous environment at low temperature, the hydrated modifications, such as rhabdophane ($LnPO_4 \cdot nH_2O$, Ln = La to Gd)[5] and weinschenkite ($LnPO_4 \cdot 2H_2O$, Ln = Dy, Y, Er, Yb or Lu)[6] are also reported.

One of the primary driving forces behind the above-mentioned applications stems from the remarkable compositional flexibility exhibited by these materials. This allows them to readily incorporate a variety of guest ions with different charges and ionic radii without significantly affecting the whole crystal lattice. For example, it has been reported that structurally homogeneous $La(Gd)PO_4$ monazite solid solutions could be experimentally synthesized by mixing La/Gd in any proportion, despite the large differences between the La^{3+} and Gd^{3+} cation radii.[9] In nature, xenotime and monazite can coexist in many igneous and metamorphic rocks, and they can form solid solutions with other minerals such as brabanite ($Ca_{0.5}Th_{0.5}PO_4$) and huttonite ($ThSiO_4$) under certain temperature and pressure conditions.[6, 10] Moreover, both xenotime and monazite are reported to experience little metamictization (a radiation-induced transformation in which the crystal structure is gradually degraded by the radiation, eventually becoming amorphous).[11] Both minerals often contain appreciable quantities of U and Th in nature, but remain stable over geological time scales despite the constant radiation exposure from the decay of these radionuclides.[10, 12] Such high structural durability and radiation resistance lead to the suggestion of xenotime- and monazite-type ceramics as potential hosts for the immobilization of long-lived high level radioactive waste.[13] In this regard, basic understanding of the resulting solid solutions, such as their structural chemistry and thermodynamic stabilities are important prerequisites for assessing their viability as a nuclear waste form.[14]

Both undoped xenotime and monazite contain only one crystallographical Ln and one P site. Their crystal structures are based on phosphate tetrahedra which are separated by interspersed rare-earth polyhedra.[12a] Each Ln^{3+} in xenotime is coordinated by eight oxygen atoms, forming a regular LnO_8 coordination geometry with two unique Ln-O bond distances, whereas a significantly distorted LnO_9 polyhedron with nine different Ln-O bond distances is observed in monazite.[14c] Consequently, the Ln^{3+} lattice site has a much higher symmetry in xenotime (D_{2d}) than in monazite (C_1).[15]

Trivalent cations may substitute directly for the Ln^{3+} host cation in the crystal lattice. In contrast, the accommodation of actinides with higher oxidation states requires coupled substitution with a mono- or divalent charge-compensating cation.[16] Additionally, a direct incorporation mechanism, based on the replacement of four Ln^{3+} by three An^{4+} and the simultaneous generation of a vacancy, was also reported in imperfect structures.[17] Yet, also the introduction of trivalent guest cations into structures, will affect the local coordination environment around the dopant's lattice site, for instance due to the differences in size and charge density between the dopant and host cations. The crucial physicochemical properties of the obtained solid solutions such as phase stability, mechanical strength and radiation tolerance will then depend on this lattice distortion.

[a] Dr. B. Xiao, H. lösch, Dr. N. Huittinen, Dr M. Schmidt
Helmholtz-Zentrum Dresden – Rossendorf, Institute of Resource Ecology
Bautzner Landstraße 400, 01328 Dresden, Germany
E-mail: moritz.schmidt@hzdr.de

The coordination geometry around the dopant will be observable as alterations in the electronic spectrum of that dopant,[18] [19] which consequently can be used to determine the local structural characteristics around a suitable dopant in the host lattice. Site-selective time-resolved laser-induced luminescence spectroscopy (TRLFS) is a sensitive spectroscopic technique responding to subtle structural alterations around a luminescent probe (here, Eu^{3+}), even when the dopant is present at trace concentration levels.[20] Eu^{3+} is the most extensively used spectroscopic probe, attributable to its high sensitivity and relatively simple luminescence spectrum.[21] To date, X-ray or neutron diffraction have been the primary means of elucidating the crystal structures. However, these crystallographic analyses tend to provide an averaged information of the whole unit cell, because they are established from least-squares fitting algorithms, which treat all ions occupying the same lattice site as one statistical average site.[22] However, such a statistical average is often not suited to accurately describe local changes induced by a guest ion in the structure of a solid solution. In contrast, different species on a given crystallographic site and the deviation of the local structure from the ideal crystallographic geometry can be directly determined and characterized by TRLFS.[23] TRLFS gives information on the geometry in the first coordination shell of the luminescent probe (Eu^{3+}), and is therefore capable of determining specific structural effects during solid solution formation, such as the local symmetry of doping sites or the number of non-equivalent species.

Recently, we have shown that Eu^{3+} may be incorporated into monazite materials independent of the host cation[24] and that full substitution is possible between the two end-members $LaPO_4$ and $GdPO_4$.[9a] Here, disorder around the dopant Eu^{3+} was found to be related to the ionic radii mismatch between Eu^{3+} and the host Ln^{3+} cation and the degree of substitution in the bulk material, respectively. In both cases highly linear trends between the excitation energy for the Eu^{3+} $^5D_0 \leftarrow {}^7F_0$ transition and the controlling bulk parameter – Ln^{3+} ionic radius and average Ln-O bond distance, or x in $La_{1-x}Gd_xPO_4$, respectively – could be established. This indicates minor deviation of the local structure from the crystallographic structure. However, due to the very low symmetry of the Ln^{3+} lattice site in the monazite structure, TRLFS is not sensitive to any additional reduction in crystal field symmetry. In this respect, doping-induced local structural distortions could not be studied in the monazite system.[24] Accordingly, it is still not clear how the local environment around guest and host ions is affected in the rare-earth orthophosphate family. For this reason, xenotime-based structures were chosen in this study. The highly symmetric rare-earth lattice site in xenotime, with a D_{2d} point symmetry, allows for sensitive characterization of any distortion of the local geometry, which is necessary to reveal the local site symmetry breakdown in rare-earth orthophophates.

In the present study, the structural effects that drive local site distortion and the periodic trends that dictate structural chemistry were systematically investigated based on six Eu^{3+} doped single crystals ($TbPO_4$, YPO_4, $HoPO_4$, $ErPO_4$ $YbPO_4$ and $LuPO_4$) from the xenotime family. Polarization-dependent site-selective time-resolved laser-induced luminescence spectroscopy (p-TRLFS) is applied to determine accurately the local structure and site symmetry of YPO_4 and $LuPO_4$. The present results are compared with those obtained for monazite counterparts, with the aim to complete and conclude systematic trends regarding trivalent dopant site symmetry in rare-earth orthophosphates.

Results and Discussion

Xenotime single crystal growth

Several fluxes were tested for the synthesis of xenotime single crystals. The most commonly used flux in these syntheses, $Pb_2P_2O_7$[25], was disregarded, due to the high probability of Pb^{2+} contamination in the product materials.[26] Tests using self-element-based fluxes, including KH_2PO_4 and $Na_4P_2O_7$, were unsuccessful and yielded only poorly crystalline or amorphous materials. Finally, we found that large crystals with well-resolved crystal faces could be isolated from an alkaline molybdate ($Na_2Mo_3O_{10}$) flux system, similar to earlier work using a mixed Na_2CO_3-MoO_3 flux to synthesize undoped monazite and xenotime crystals.[27]

Six Eu^{3+} doped xenotime materials, $TbPO_4$, YPO_4, $HoPO_4$, $ErPO_4$, $YbPO_4$ and $LuPO_4$, were successfully grown. Attempts to prepare the Eu^{3+} doped $DyPO_4$ and $TmPO_4$ crystals under various experimental conditions, including excess of flux and several different temperature profiles, were not successful. It cannot be easily explained why our attempts to produce crystals of these two materials, which do not represent the extremes of this series, but rather are found in between materials which could be synthesized, were unsuccessful. However, these difficulties in obtaining crystals of some materials may be a first indication that Eu^{3+}'s driving force to be incorporated into xenotime matrices is low and for the complicated incorporation behavior of Eu^{3+} into xenotime structures.

Incorporation of Eu^{3+} ions into xenotime

Excitation spectra of the $^5D_0 \leftarrow {}^7F_0$ transition of six Eu^{3+} doped xenotime crystals ($TbPO_4$, YPO_4, $HoPO_4$, $ErPO_4$ and $LuPO_4$) are shown in **Figure 1**. The recorded spectra cover the appropriate energy region from 573 to 582.5 nm (17452 to 17167 cm^{-1}). The excitation spectra are very similar to each other with some deviation for $LuPO_4$. The spectra of $TbPO_4$, YPO_4, $HoPO_4$, $ErPO_4$, and $YbPO_4$ all contain one sharp feature at 580.7 – 580.8 nm (17217 – 17220 cm^{-1}), the peak position varies by only 3 cm^{-1} for these five materials. We will refer to the Eu^{3+} species excited at this wavelength as species A. The excitation peaks are generally sharp, but the full width at half maximum (FWHM) varies unsystematically for the materials. The largest FWHM is found for $HoPO_4$ (16.30 cm^{-1}), and for $TbPO_4$ a very sharp feature (1.32 cm^{-1}) is found to sit on top of a broader peak (~20 cm^{-1}). The peak position of species A shows a strong bathochromic shift in $LuPO_4$, where the excitation maximum is observed at 582.0 nm (17,182 cm^{-1}). Such a shift must indicate a

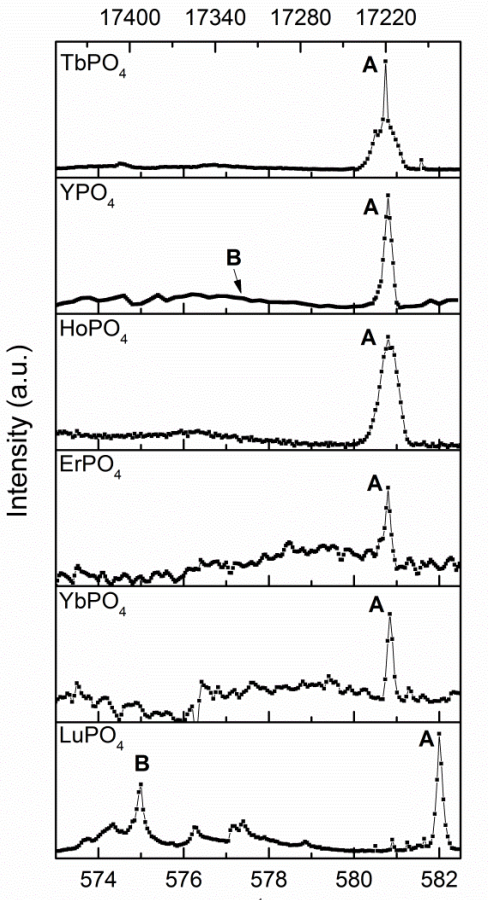

Figure 1. Excitation spectra of six Eu^{3+} doped xenotime crystals ($TbPO_4$, YPO_4, $HoPO_4$, $ErPO_4$ and $LuPO_4$).

significantly stronger crystal field around the Eu^{3+} dopant in $LuPO_4$. The peak exhibits a similar FWHM as in the other materials, here 4.72 cm^{-1} (see **Table 1**).

In the spectrum of Eu^{3+}-doped $LuPO_4$ we also observe a second sharp transition at 575.0 nm (17391 cm^{-1}). In the same spectral range, roughly from 573 to 580 nm (17454 to 17241 cm^{-1}), we observe very broad unstructured bands with low intensity in all other materials. We will refer to any species excited in this range as species B.

For species A, the occurrence of a narrow peak in each host denotes a well-defined crystalline lattice site for Eu^{3+} incorporation into the structures. Based on the crystal structure of xenotime we can assume species A represent Eu^{3+} incorporation on the Ln^{3+} lattice site. The same substitution had been observed in monazite $LnPO_4$.[24] However, the details of the incorporation behavior are rather different. For monazite ceramics, systematic trends in both excitation peak position and FWHM had been observed throughout the solid solution series.[24] In contrast, for the xenotime ceramics no such trend is discernable. Instead, the same peak position is found for five of the studied materials with very high precision and the FWHM appears to be randomly distributed (**Table 1**). Finally, for $LuPO_4$ the peak position shifts by ≥ 35 cm^{-1} relative to the other materials. The bathochromic shift of the $^5D_0 \leftarrow {}^7F_0$ transition is associated with the strength of the crystal field around Eu^{3+},[20] while its peak width is typically related with structural disorder around the cation.[9a, 28] We thus find two distinctly different coordination environments for species A, one with a relatively weak crystal field and varying structural disorder ($TbPO_4$ – $YbPO_4$) and one with a significantly stronger crystal field and average structural disorder ($LuPO_4$).

A bathochromic shift of 38 cm^{-1} from $TbPO_4$ to $LuPO_4$ is quite significant. We can use the formalism established by Albin and Horrocks Jr. to correlate the peak positions to an effective charge of the ligands.[29] Using the equation as cited in,[20] the effective charge *p* increases by more than 25% from $TbPO_4$ to $LuPO_4$ (*p* = 10.0 and 12.6, respectively). As the charge is not likely to change in the crystalline matrix, it appears reasonable the spectral shift is related to changes in bond distance. We can use the equation established recently for monazite ceramics, so in the same chemical system, to estimate Eu – O bond distances in our materials. For $TbPO_4$ and $YbPO_4$ we calculate nearly identical bond distances of 2.24 Å and 2.23 Å, respectively. These values are shorter than the crystallographic bond distances (avg. Ln – O bond distances of 2.365 Å and 2.313 Å, respectively), which is likely an effect of the lower coordination number in xenotime compared to monazite. It is however noteworthy that the difference in calculated Eu – O bond distances (0.01 Å) is actually significantly smaller than the crystallographically expected values (0.052 Å). This would indicate that in the xenotime ceramics of the earlier lanthanides the Eu^{3+} coordination sphere is not directly controlled by the host's crystallographic structure. In contrast, we calculate a Eu – O bond distance of 2.06 Å for Eu^{3+} in $LuPO_4$, once again a too small value due to the different coordination number, but more than 0.15 Å shorter than calculated for the other xenotime solid solutions using the same equation. The bond distance difference between crystallographic $LuPO_4$ and $TbPO_4$ on the other hand is

Table 1. FWHM values and peak positions of A species in both monazite- and xenotime-structures. The values for the monazite structures are taken from Huittinen et al. 2016[24]

samples	Ln-O[6]	excitation peaks for A species		FWHM
	(Å)	(nm)	(cm^{-1})	cm^{-1}
$LaPO_4$	2.579	578.40	17289	1.03
$SmPO_4$	2.499	578.94	17273	0.95
$EuPO_4$	2.488	579.01	17271	-
$GdPO_4$	2.476	579.11	17268	0.92
$TbPO_4$	2.365	580.73	17220	1.32
YPO_4	2.345	580.79	17218	7.11
$HoPO_4$	2.343	580.8	17218	16.30
$ErPO_4$	2.329	580.81	17217	4.15
$YbPO_4$	2.313	580.82	17217	4.15
$LuPO_4$	2.302	582.00	17182	4.72

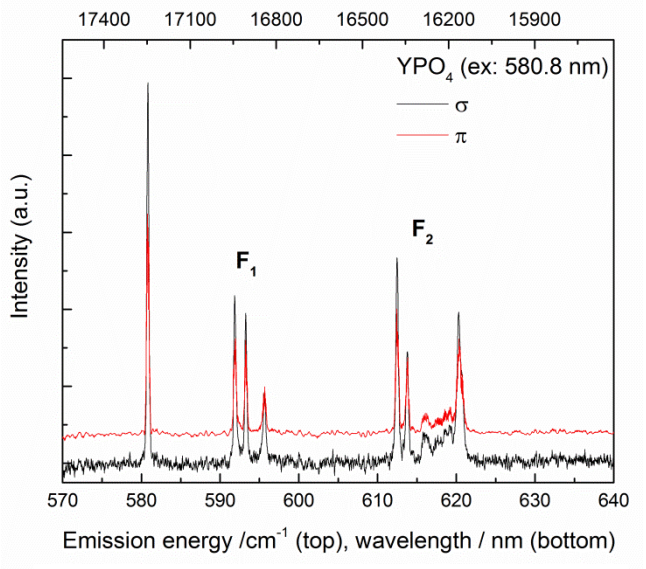

Figure 2. The polarized emission spectra of species A (selectively excited at 580.8 nm/17218 cm^{-1}) in YPO_4.

merely 0.065 Å, less than half the calculated difference. This drastic change may be caused by the formation of a covalent bond between PO_4^{3-} and Eu^{3+}, possibly due to forced orbital overlap in the too small Lu^{3+} lattice site of $LuPO_4$ xenotime.

An identification of species B is less straightforward. It appears two different processes may contribute to excitation features in the same spectral region: a distinct second species, as well as an energy transfer or hot band. A hot band would be related to vibronic transitions,[30] in which vibrational modes, e.g. lattice phonons are excited jointly with the electronic transitions, while an energy transfer band would involve excitation via a second ion,[28] most likely the host lanthanide. The latter can be excluded in the two phases where the host cation does not possess valence electrons that could be excited in the spectral range of our experiments, i.e. YPO_4 and $LuPO_4$. Both a hot band and an energy transfer process would lead to the observation of the emission spectrum of species A, and will be discussed with the emission spectra in the next section.

Breakdown of crystallographic site symmetry in xenotime

In order to examine the specific local environment of species A and B, p-TRLFS spectra in σ and π polarization geometry were recorded after selective excitation. For reference, σ spectra are recorded with the electric vector *E* perpendicular to the optical axis, and π spectra are measured with electric vector *E* parallel to the optical axis. Here, we will focus on the luminescence spectra of YPO_4 and $LuPO_4$, because the other materials potentially exhibit host-dopant energy transfer, which will complicate the interpretation of measured spectra. All the recorded luminescence spectra cover the $^5D_0$ to ^7F_J (J = 0 − 4) transition range (see **Figure S4**). Among these, the number and polarization characterization of the $^5D_0 \rightarrow {}^7F_J$ (J = 1, 2) transitions have proven to be the most useful in the determination of the Eu^{3+} ion site symmetry, because of their high intensity and clear resolution.[31]

A. YPO_4

The polarized luminescence spectra of species A (selectively excited at 580.8 nm/17218 cm^{-1}) are shown in **Figure 2**. The spectral profiles of both σ and π geometries are almost identical. The $^5D_0 \rightarrow {}^7F_0$ transition shows one peak, in agreement with a single species being excited. Three transition peaks are seen in the $^5D_0$ to $^7F_1$ manifold, which indicates Eu^{3+} occupies a low symmetry site. The $^5D_0 \rightarrow {}^7F_2$ transition contains three clearly resolved peaks accompanied by weaker lines barely above noise level. We conclude that the number of $^5D_0 \rightarrow {}^7F_J$ transitions are 1, 3 and 5 for J = 0, 1, and 2, respectively. According to the selection rules,[32] the complete lifting of the 2J+1 degeneracy of $^7F_{1,2}$ levels and the absence of any polarization effect is in accordance with C_1 site symmetry. In either case, it is obvious that the dopant Eu^{3+} site suffers a significant local structural distortion that perturbs the site symmetry from the crystallographic D_{2d} to C_1. This splitting pattern is similar to that of monazite-based $LnPO_4$ (Ln = La − Gd),[24] in which Eu^{3+} exhibits C_1 dopant site symmetry for all members. The luminescence spectra in both cases exhibit the same splitting patterns but different intensity distributions, both with respect to the relative intensities of J-sublevels and F_1/F_2 intensity ratio. In this regard, species A in YPO_4 experiences an equally low symmetry due to local distortion as in the monazite counterparts, but the corresponding local environment of Eu^{3+} dopant is distinct from the monazite structure.

When species B is excited selectively at 577.5 nm (17316 cm^{-1}), as shown in **Figure 3**, the luminescence spectra show a very weak luminescence making an unambiguous determination of splitting patterns impossible. Nevertheless, it is clear that the recorded spectra are different from those of species A and that

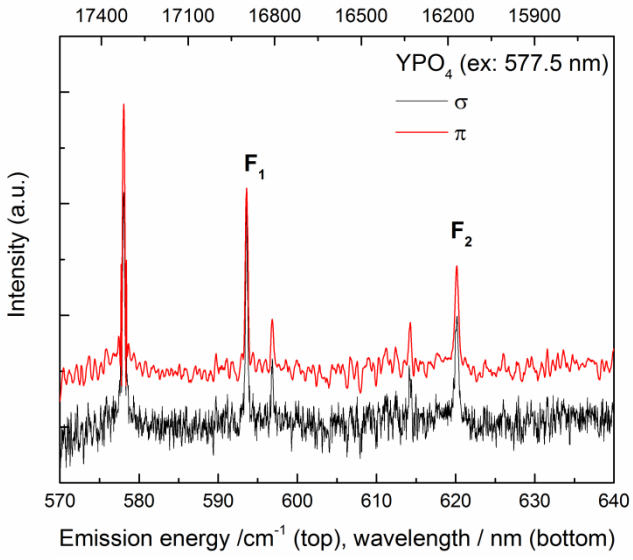

Figure 3. Polarized emission spectra of species B (selectively excited at 577.5 nm in YPO_4

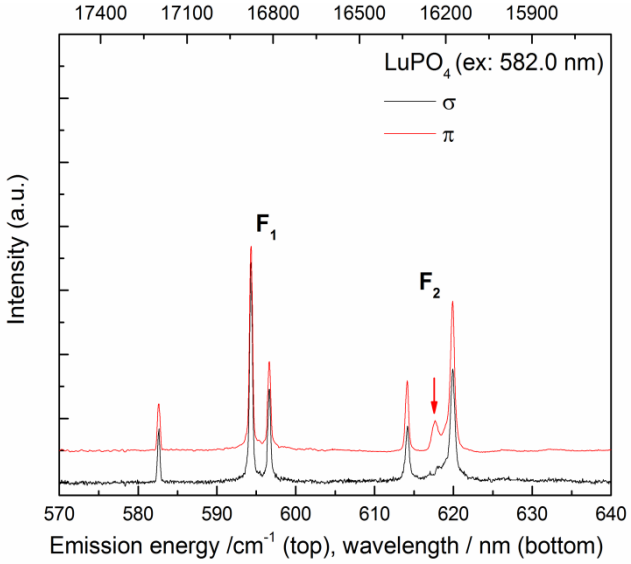

Figure 4. Polarized emission spectra of species A (selectively excited at 582.0 nm/17182 cm^{-1}) in $LuPO_4$. The red arrow indicates the most obvious polarization position.

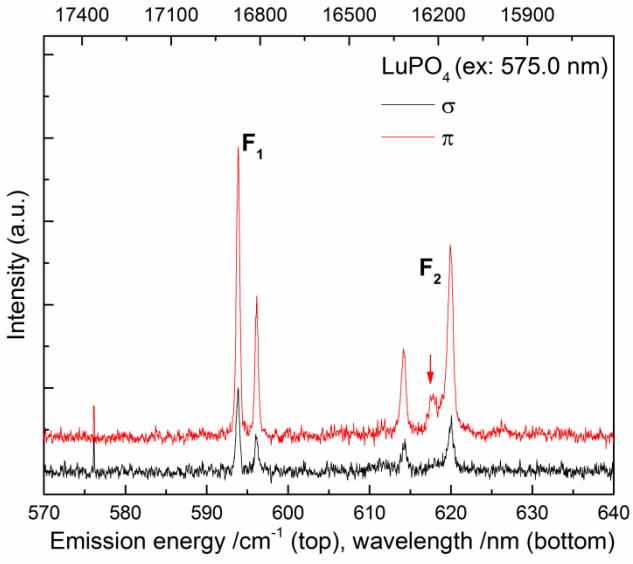

Figure 5. Polarized emission spectra of "species B" (selectively excited at 575.0nm /17391 cm^{-1}) in $LuPO_4$. The red arrow indicates the most obvious polarization position.

they show no polarization dependency. Comparing relative intensities of J-sublevel transitions and the overall ratio of ($^5D_0 \rightarrow {}^7F_1$) to ($^5D_0 \rightarrow {}^7F_2$) transition reveals clear differences between A and B. For example, in the case of the hypersensitive F_2 band, the strongest peak for species B is located at ~620 nm, while the most intense peak is found at lower wavelength ~612 nm for species A. The calculated ($^5D_0 \rightarrow {}^7F_1$)/($^5D_0 \rightarrow {}^7F_2$) intensity ratio of species B with a value of 1.21 is also not comparable with that of species A (0.82). In this case, we can then conclude that species B is indeed a distinct species in the YPO_4 lattice, any further characterization is however restricted by the low luminescence intensity of species B. Excitation at two additional wavelengths in the spectral range of species B yield identical emission spectra, but no improvement in luminescence intensity.

B. $LuPO_4$

As discussed previously, for $LuPO_4$, both species A and B exhibit one sharp peak in the corresponding range of the excitation spectrum. The luminescence spectra, recorded after selective excitations at 582.0 nm (17182 cm^{-1}) and 575.0 (17391 cm^{-1}) for species A and B are shown in **Figure 4** and **Figure 5**, respectively. The spectra are essentially identical to each other, but demonstrate different splitting patterns and polarization dependence compared to those of YPO_4. Unlike YPO_4, in which none of the observed peaks exhibits any distinguishable polarization dependence, the luminescence of both A and B species for $LuPO_4$ have a pronounced dependence on the polarization, indicating a higher symmetry of the local coordination environment for the dopant Eu^{3+}.

In the case of species A, both polarization geometries have one line in the $^5D_0 \rightarrow {}^7F_0$ transition and two lines in the $^5D_0 \rightarrow {}^7F_1$ transition. Again, the one relatively sharp peak in the F_0 band shows that a single species is excited. The observation of only two-fold splitting implies a higher site symmetry, compared to three splitting lines found for its YPO_4 counterpart. Polarization dependence becomes manifest in the $^5D_0 \rightarrow {}^7F_2$ transition: in π geometry, three lines are clearly resolved, composed of one weak and two stronger peaks, while in σ geometry, the weakest peak in the same band disappears reducing the multiplicity from three to two, as highlighted by in **Figure 4**. In the case of the F_4 band, both polarization geometries exhibit similar three-fold splitting patterns. Taken together, total number of (1σ, 1π), (2σ, 2π), (2σ, 3π) and (3σ, 3π) transition peaks are counted for $^5D_0$ to F_0, F_1, F_2, and F_4 transitions (see SI for J = 3, 4), respectively.

Eu^{3+} ions substituting Lu^{3+} host cations in $LuPO_4$ would ideally occupy a crystallographic site with D_{2d} point symmetry. In this ideal environment, the $^5D_0 \rightarrow {}^7F_2$ and $^5D_0 \rightarrow {}^7F_4$ transitions would produce (1σ, 1π) and (2σ, 1π) emission lines. Clearly, the appearance of additional peaks in F_2 and F_4 bands in $LuPO_4$ infers that the coordination environment of Eu^{3+} undergoes a local distortion. A straightforward assignment of a point group to Eu^{3+} in $LuPO_4$ is problematic, as the observed pattern does not match any found in the literature. Possible explanations could be an incomplete polarization of the exciting laser light, or not resolved additional lines in the spectra. Both seem unlikely however. On the one hand, should the use of inherently polarized laser light (> 80%) in combination with two polarization filters ensure a very high degree of polarization (> 99%). On the other hand, all observed lines in the emission spectra are extremely sharp and generally well resolved with baseline intensity between peaks. The explanation must then lie in the coordination environment of Eu^{3+} itself. It appears that the coordination environment is sufficiently distorted from the crystallographic D_{2d} point symmetry to exhibit a different splitting pattern, while some degeneracy remains within our experimental limitations. The observed splitting pattern bears largest

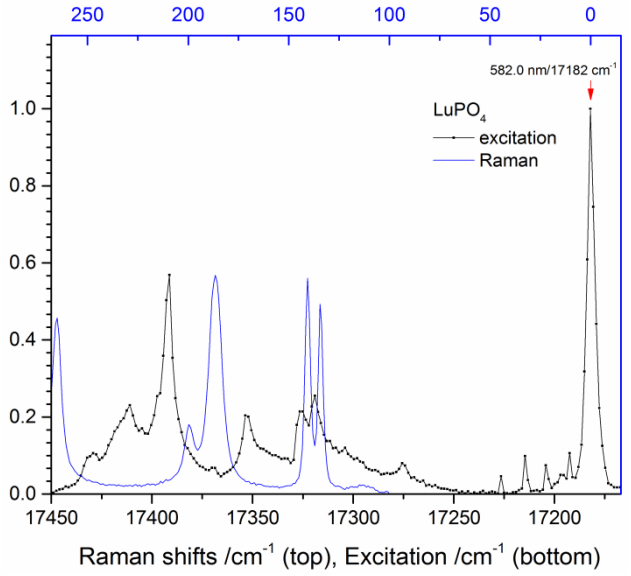

Figure 6. Combined excitation spectra and the Raman spectra for $LuPO_4$ (normalized stokes-shift of the Raman spectra adjusted to the excitation energy of the TRLFS spectra). The complete Raman spectrum for $LuPO_4$ is shown in Figure S6.

resemblance to the theoretically derived transitions from S_4 symmetry, but does not exhibit a perfect match, which would show a $^7F_2$ splitting of (1σ, 2π), which is obviously not the case here. Nonetheless, D_{2d} symmetry partially distorted toward S_4 is a reasonable assignment for Eu^{3+} ion site symmetry. It is worth mentioning that similar distortions have been previously observed in Eu^{3+} doped $CaWO_4$ single crystals.[28] Independent of the specific point symmetry of the Eu^{3+} lattice site, it is evident that less distortion is induced in the $LuPO_4$ lattice than in YPO_4 upon incorporation of Eu^{3+}, despite the much larger mismatch in cation size in the former case.

Once again in contrast to YPO_4, species B in $LuPO_4$ exhibits the same emission spectrum as species A. Both polarization geometries also have transition lines of (1σ, 1π), (2σ, 2π), (2σ, 3π) and (3σ, 3π) for $^5D_0$ to F_0, F_1, F_2, and F_4 transitions, respectively. This indicates that species B in $LuPO_4$ is not a distinct species but a hot band of species A, energy transfer via Lu^{3+} seems unlikely due to its $4f^{14}$ electron configuration. The appearance of species B as a sharp peak rather than a broad continuous band suggests that it is a vibronic transition. Moreover, the spectral distance of ~210 cm^{-1} is in reasonable agreement with the excitation of a lattice phonon that is coupled with $^5D_0 \rightarrow F_0$ transition. In order to substantiate this, we plot the excitation spectrum of $LuPO_4$ together with its excitation energy adjusted Raman shifts. As shown in **Figure 6**, the high energy region including species B and the energy range of lattice phonons overlap. The overlap indicates an excitation process involving lattice phonons to the $^5D_0$ - $^7F_0$ transitions of Eu^{3+} species A. There is no direct overlap of "species B's" most intense band at $\Delta E = 210$ cm^{-1}, but the most intense Raman band in this energy range is shifted by only 24 cm^{-1}. Such an energy shift seems reasonable upon substitution of Lu^{3+} by Eu^{3+} on the same lattice site. Following the assignment of lattice vibrations in Poloznikova and Fomichev[33] for $LuPO_4$, these low-energy phonons are attributed to external translations (E_g and B_{1g}) of the $(PO_4)^{3-}$ and Lu^{3+} ions.

Incorporation effects on YPO_4 and $LuPO_4$

From the above it becomes clear that the YPO_4 structure becomes significantly more perturbed than the $LuPO_4$ structure. Not only do we find a significantly stronger distortion of the main Eu^{3+} species A from the crystallographic symmetry in YPO_4, there is also an additional lattice site with a significantly weaker crystal field, which is not observed in $LuPO_4$. This observation is somewhat counterintuitive, as the ionic radii mismatch, a common parameter for the prediction of solid solution stability,[34] would suggest a higher stability of the YPO_4:Eu^{3+} solid solution ($\Delta(^{VIII}Y^{3+}, {}^{VIII}Eu^{3+}) = 4.6\%$)[35] than its $LuPO_4$:Eu^{3+} equivalent ($\Delta(^{VIII}Lu^{3+}, {}^{VIII}Eu^{3+}) = 9.1\%$).[35] The explanation for the observed behavior must then be related to the structural flexibility in the two systems. Our data suggest very similar coordination environments in the xenotime structures of all the larger rare earth cations, despite a wide range of ionic radii from Tb^{3+} ($r^{VIII}(Tb^{3+}) = 1.040$ Å)[35] to Yb^{3+} ($r^{VIII}(Tb^{3+}) = 0.985$ Å)[35]. In all these systems introduction of Eu^{3+} ($r^{VIII}(Eu^{3+}) = 1.066$ Å)[35] into the lattice will disturb the regular structure and induce local relaxations. The resulting local environment appears to be indifferent to the original lattice structure, and rather form some optimum coordination environment for Eu^{3+} in the xenotime structure. We suggest that in $LuPO_4$, the lattice with the largest size mismatch of host and guest cation, the crystal lattice is not sufficiently flexible to accommodate Eu^{3+} in this same environment. Instead, the observed high symmetry and extreme bathochromic shift show that Eu^{3+} is forced into a coordination environment very similar to the crystallographic lattice site, with PO_4^{3-} ligands in very close proximity. This may also explain the well-resolved coupling of Eu^{3+} electronic transitions to $LuPO_4$ lattice phonons.

Comparison of Eu^{3+} incorporation in monazite and xenotime

Rare-earth orthophosphates $LnPO_4$ (Ln = La – Lu, Y) with xenotime or monazite structures contain only one crystallographically unique Ln site each, having the simplest chemical and structural configuration among rare-earth phosphates. However, the spectroscopic data presented here for xenotime combined with previous research on monazite[9a, 24] demonstrate that the incorporation of Eu^{3+} proceeds rather differently in these two materials. In the case of monazite, a homogeneous solid solution series was found with systematic linear trends in the spectroscopic features. Despite very similar relative sizes, the incorporation into xenotime, where the host cation is smaller than the guest cation is significantly more complex. Our data demonstrate that the local structure around the Eu^{3+} dopant mainly depends on the host lattice's flexibility. In such a way that lattices with larger host cations, which need less flexibility to accommodate Eu^{3+}, will do so in a strongly distorted lattice site, while the relatively largest distortion in $LuPO_4$ is no longer observed and Eu^{3+} is instead incorporated on a significantly more symmetrical lattice site.

Conclusions

We have demonstrated the effect of the incorporation of Eu^{3+} into xenotime single crystals on the molecular level. Despite appearing as single-crystalline xenotime in XRD experiments, spectroscopic investigations clearly show that the local structure around a dopant ion may vary quite significantly from the ideal crystal structure. We find two regimes for the incorporation, substitution of Eu^{3+} for REE^{3+} on a highly distorted lattice site for the materials with larger cations and substitution into an only marginally distorted lattice in $LuPO_4$. We suggest this difference in the substitution can be explained by the host lattices' flexibility and required motion to accommodate the larger guest cation. In the case of $LuPO_4$, a site symmetry akin to S_4 is found, which can be obtained from the crystallographic D_{2d} by a slight distortion of the crystal field. For example, rotation of the PO_4^{3-} trigonal prisms, would lead to the loss of the dihedral reflection plane (σ_d) that is parallel to the main twofold rotation axis and result in a site with S_4 symmetry, as shown in **Figure 7**. Our results illustrate that selecting a host material for a solid solution for any technical application will require careful characterization of local effects in the host structure, which may not be easily predicted based on bulk parameters such as the ionic radius mismatch. With respect to the immobilization of radionuclides from specific waste streams in ceramic matrices, it appears reasonable to conclude that monazite host phases with cations larger than the ions to be incorporated should be more amenable to the incorporation of large quantities of dopants than the xenotime materials studied here. To validate this conclusion, these findings need to be verified in polycrystalline systems more similar to the technically relevant ceramics and the long-term stability of such phases should be characterized.

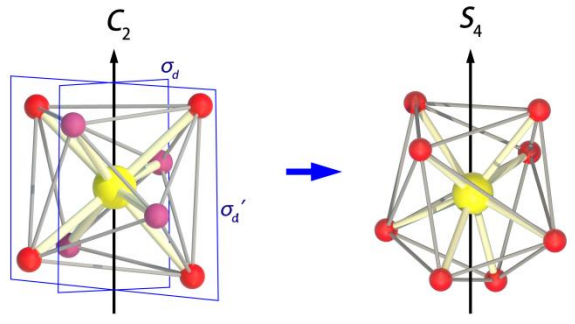

Figure 7. Possible distortion of D_{2d} to S_4 point symmetry. Rotation of the trigonal prisms leads to the loss of dihedral reflection plan (σ_d) that is parallel to the main twofold rotation axis and result in a site with S_4 symmetry

Experimental Section

Syntheses

Our synthetic strategy is to obtain bulk xenotime single crystals, large enough in volume with well-resolved crystal faces, which are suitable for the polarization-dependent luminescence spectroscopy experiments. The xenotime single crystals used in this work were obtained in two steps. First, we synthesized pure xenotime polycrystalline samples. Then, we used them as precursors in the second step for growing the bulk single crystals. All the raw materials in this synthesis section are fine powders, which are commercially available with analytic purity.

Syntheses of xenotime polycrystalline samples (Step 1)

Polycrystalline xenotime precursors were synthesized by a precipitation method. The detailed experimental procedures for this step are described in the literature,[9a] and are only briefly summarized here. Stoichiometric amounts of $Ln(NO_3)_3{\cdot}6H_2O$ and H_3PO_4 (with molar ratio = 1:1) were dissolved in distilled water with appropriate amounts of Eu_2O_3 at ambient conditions. The concentration of Eu^{3+} is chosen, so that the amount of Eu^{3+} in the final product is 200 ppm relative to the host Ln^{3+} cation, if all Eu^{3+} becomes incorporated into the xenotime product. The chemical reactions for these raw materials will lead to rare-earth precipitates according to Reaction (1):

$$Ln(NO_3)_3{\cdot}6H_2O + H_3PO_4 \xrightarrow{200\ ppm\ Eu^{3+}} LnPO_4{:}Eu^{3+}(precipitate) + 3HNO_3 \quad (1)$$

After recovering the precipitate by centrifugation and decanting excess fluid, the precipitate was dried at 600 °C for 2h without any further treatment, such as mortaring to evaporate water and other volatiles. The precipitate was then sintered at 1450 °C for 5h to yield the polycrystalline xenotime products. The as-synthesized polycrystalline precursors were collected and their purity was characterized by powder XRD investigations (see support information of **Figure S1**). All powder XRD profiles confirmed the presence of xenotime and no reflexes indicating the presence of monazite or any other phases were observed. Details on the PXRD set-up are given below.

Growth of xenotime single crystals (Step 2)

Due to the high melting point (*Hikichi* determined that xenotime melts above 2000 °C),[36] single crystals of xenotime are extremely difficult to be obtained through directly melting the corresponding polycrystalline materials. Therefore, we used the flux growth method to grow the xenotime single crystals. By using this technique, the polycrystalline xenotime obtained from step 1 could be dissolved in a molten flux of sodium trimolybdate ($Na_2Mo_3O_{10}$) at a relatively low temperature, and then re-crystallized to form single crystals during slow cooling procedure.[37]

The detailed crystal growth conditions and optimized ratios between solutes and solvents are summarized in **Table 2**. For a typical

Table 2. Conditions for single crystal growth of xenotime.

Crystals	Starting materials (g)	Holding T (°C)	Holding time (h)
$TbPO_4$	$TbPO_4$(2.00) + $Na_2Mo_3O_{10}$(194.49)	1350	15
YPO_4	YPO_4(2.00) + $Na_2Mo_3O_{10}$(268.55)	1330	18
$HoPO_4$	$HoPO_4$(2.00) + $Na_2Mo_3O_{10}$(189.99)	1350	15
$ErPO_4$	$ErPO_4$(2.00) + $Na_2Mo_3O_{10}$ (188.31)	1350	15
$YbPO_4$	$YbPO_4$(2.00) + $Na_2Mo_3O_{10}$(184.24)	1280	20
$LuPO_4$	$LuPO_4$(2.00) + $Na_2Mo_3O_{10}$(182.93)	1300	20

experiment, a platinum crucible containing polycrystalline $LnPO_4$ and $Na_2Mo_3O_{10}$ flux (at a molar ratio of 1: 50) was placed in the center of a vertical, programmable temperature furnace (Fuzhou KLST Test Equipment Co., P.R. China). The mixture was heated to 1350 °C and held for 15 h to ensure complete dissolution of the raw materials. The cooling rate for the $LnPO_4$ re-crystallization was 4 °C/h from 1350 to 870 °C (little crystallization of $LnPO_4$ occurred below 870 °C under such crystal growth condition). Subsequently, the furnace temperature was rapidly (20 °C/h) cooled down to 400 °C followed by quenching. After each experiment, the resulting products were $LnPO_4$ crystals embedded in a matrix of solidified molybdates. The grown single crystals were easily separated from the molten flux by repeatedly washing with hot water. The morphology of all grown xenotime crystals was an elongated bipyramid. **Figure S2** shows a typical crystals obtained by this method.

Powder XRD and single-crystal structure analyses

The obtained polycrystalline samples from step 1 and the crystals from step 2 were examined by laboratory source powder and single-crystal X-ray diffractions, respectively. X-ray powder diffraction patterns were collected on a Rigaku MiniFlex diffractometer, equipped with a 600 W X-ray source tube (λ = 1.54187 Å) and 6-position automatic sample changer. Data were recorded in the range of 2θ = 10−80° (total counting time = 10 s/step with a step width of 0.02°) and analyzed using data given in the PDF-2 cards.[38] The X-ray powder diffraction patterns for all studied samples are provided in the Supporting Information (**Figure S1**). All samples can be unambiguously identified as the desired materials, and show no reflections not associated with the xenotime structure.

As-grown Eu^{3+}-doped xenotime single crystals were analyzed on a Bruker D8 VENTURE diffractometer with a PHOTON 100 CMOS detector at room-temperature using microfocused Mo Kα radiation (λ = 0.71073 Å). Suitable single crystals were selected under a polarizing optical microscope and glued on a glass fiber for SC-XRD experiments. More than a hemisphere of data was collected for each crystal, and the three-dimensional data were reduced and filtered for statistical outliers using the APEX3 program. Data were corrected for Lorentz, polarization, absorption, and background effects. The SHELXL-97 program was used for the determination and refinement of the structures.[39] The results of the single-crystal structural analysis show that the rare-earth site crystallizes exclusively in D_{2d} site symmetry for all the xenotime crystals. The obtained Eu^{3+}-doped xenotime single crystals have crystal shapes identical to similar compounds produced by other methods in the literature.[40] Both, powder and single crystal XRD showed patterns typical for highly crystalline materials with no discernible deviation from the respective ideal structure of the pure materials.

Raman spectroscopy

Raman measurements on grinded YPO_4 and $LuPO_4$ single crystals at room temperature were performed on a LabRam ARAMIS (Horiba Jobin Yvon) using a Nd:YAG laser with an excitation wavelength of 532 nm which was calibrated on a silicon single crystal. For spectral splitting a spectrograph with a 1800 lines/mm grating was used. The entrance slit was set to 100 µm with a hole of 300 µm. For all measurements a neutral density filter D 0.3 (50 % transparency) was used. The peaks of interest are located between 100 and 1300 cm^{-1}.

Laser-induced luminescence spectroscopy (p-TRLFS)

Eu^{3+} TRLFS is a versatile tool that can respond to small structural differences for a luminescent center in solids, solutions, and at interfaces.[41] The optical properties of Eu^{3+} are largely governed by its local coordination environment, and the luminescence of Eu^{3+}-doped materials is critically dependent on the crystal-field surrounding the Eu^{3+} emitters. The use of optical spectra of Eu^{3+} in solving complex problems in solid-state chemistry has been studied extensively and reviewed thoroughly.[20, 23, 42] Here, a brief description of Eu^{3+} luminescence properties as well as experimental setup required for our experiments is given below.

The Eu^{3+} environment in crystalline structures can be obtained from the combined excitation ($^5D_0 \leftarrow {}^7F_0$) and luminescence emission ($^5D_0 \rightarrow {}^7F_J$, J = 1, 2) spectra. Excitation spectra are obtained by integrating the luminescence intensity as a function of the excitation wavelength. Therefore, the resolution is not limited by the resolution of the detector but only by the tuning resolution of the laser system (< 0.01 nm, see below). For the excitation from the $^7F_0$ ground state to the $^5D_0$ state, no peak splitting is observed, due to the fact that both $^7F_0$ and $^5D_0$ states are non-degenerate. Whenever several lines are observed for the $^5D_0 \leftarrow {}^7F_0$ transition, this indicates that Eu^{3+} ions are located in sites with different local environments (different species). The number of the $^5D_0 \leftarrow {}^7F_0$ transition lines in the excitation spectra is then the number of non-equivalent Eu^{3+} species. Furthermore, selective excitation of each of the Eu^{3+} species to the $^5D_0$ state by a tunable laser yields luminescence emission spectra of each single species. The splitting patterns of the $^5D_0 \rightarrow {}^7F_1$ and $^5D_0 \rightarrow {}^7F_2$ transitions give certain information on the site symmetry of the Eu^{3+} ions. As mentioned above, the non-degenerate $^5D_0$ state cannot split in a crystal field, thus the spectral splitting arise from the lower ^7F_J states. The extent to which the degeneracy of $^7F_1$ and $^7F_2$ sublevels is reduced depends on the crystal-field perturbation on the luminescent Eu^{3+} ions.[20]

In this study, polarization-dependent (p-TRLFS) experiments were performed for xenotime single crystals. All samples were cooled to low temperature (T < 10 K) using a helium refrigerated cryostat (Cryophysics CCS 100) to obtain the spectral resolution required to discriminate different crystal-field transition lines of Eu^{3+}. The crystals were oriented and mounted on a sample holder behind two polarizers so that polarized luminescence signals could be recorded when excited by a tunable dye laser. In a typical polarization-dependent setup, the luminescence signals were recorded along two polarization directions, namely, σ and π, relative to the crystal's optical axis. **Figure S3** shows the setup of the π-polarized luminescence experiment. The excitation laser beam emitted from the dye laser is polarized with its electric vector (*E*) parallel to the direction of the z-axis. The polarized beam is monitored by a polarizer (Glan-Laser Calcite Polarizer) and then reflected at a right angle by a prism. After turning, the incident light propagates along the z-axis with its electric vector parallel to the x-axis. Spectra were recorded with light propagating transverse to the crystallographic *c*-axis of each crystal sample. The π spectrum is determined with the *E* vector parallel to the *c*-axis, whereas the σ spectrum is defined by *E* perpendicular to the *c*-axis.

The laser luminescence was excited using a Nd:YAG system (Continuum Surelite II, USA) pumped dye laser (Radiant Dyes NarrowScan K). Rhodamine 6G was used as a dye for direct excitation of Eu^{3+} ions from the ground $^7F_0$ state to the emitting $^5D_0$ state (from 575 to 582 nm). The laser wavelength was monitored with a wavelength meter (High Finesse WS-5), and the laser energy was monitored using an optical power meter (Newport 1918-R). Luminescence signals were recorded from a spectrograph (Shamrock 303i) equipped with a polychromator with 300, 600 and 1200 lines/mm gratings and an intensified CCD detector (Andor iStar 734). Before the measurement, the grating was calibrated from the emission lines of a neon lamp. In order to minimize the effect of the laser pulse on the spectra, the minimum gate delay between laser pulse and camera gating was set to 1.0 µs. The gate width of the camera was fixed at 10 ms to ensure the collection of the entire luminescence signal. For lifetime measurements, the luminescence emissions were collected using a varied delay time from 15 to 50 µs with a total up to 75 steps.

Crystal orientation and dopant site symmetry determination

Different Eu^{3+} site symmetries in crystal lattice give rise to different characteristic spectral splitting patterns. Consequently, luminescence spectra recorded for *f-f* transitions of the Eu^{3+} ion are a reflection of the local structural details in that crystalline lattice. Details on the experimental setup required to determine the local dopant site symmetry are available in the literature.[28] Polarization effects are based on the property of an anisotropic crystal that a transition is permitted only in certain crystallographic direction while it is forbidden in the other directions, and can give additional information on the local structure of a luminescence center.[20] Anisotropic crystals have crystallographically distinct axes and interact with light non-uniformly, depending on the orientation of the light's field vectors relative to this crystallographic axis. For a uniaxial crystal like xenotime, where two out of the three crystallographic axes are interchangeable, light still behaves isotropically when propagating along the optical axis (the non-interchangeable axis, here the *c*-axis), but the observed transitions and splitting patterns will be affected when light propagates in any other direction. With the aid of selection rules, the polarization characteristics of emission lines which originate from transitions between different crystal-field levels of the Eu^{3+} ions can be used to deduce the local site symmetry.[43]

In order to perform the polarization-dependent spectroscopic experiment, it is important to know the direction of the crystal's optical axis relative to the laser's propagation direction. The optical axis of a uniaxial crystal like xenotime can be determined by combination of crossed polarizers and x-ray diffraction techniques.[44] First, the plane containing or perpendicular to the optical axis could be found with two crossed polarizers. After this, the crystals are glued on a sample holder and the Miller indices of the crystal faces can be determined by X-ray diffraction. Typically, this requires sophisticated analysis to correctly record the orientation of the optical axis with respect to the turning axis, especially for tiny crystals. For the large crystals synthesized in this study, optical axes can often simply be determined through comparison of the faces with those of a simulated model. Depending on the orientation of the crystal lattice with respect to the incident light's polarization plane, the observed anisotropic emission effects vary between two extreme situations, with the directions of the light's electric vector perpendicular (σ polarization) or parallel (π polarization) to the crystallographic-*c* axis.

Acknowledgements

Special thanks are given to Dr. Atsushi Ikeda (Institute of Resource Ecology, Helmholtz-Zentrum Dresden-Rossendorf) for assistance in the use of single crystal and powder XRD equipment. We gratefully acknowledge the Helmholtz Gemeinschaft Deutscher Forschungszentren for funding the Helmholtz-Nachwuchsgruppe "Structures and Reactivity at the Water/Mineral Interface" (VH-NG-942).

Keywords: Xenotime • Incorporation • TRLFS • Luminescence • Eu^{3+}

[1] P. Yang, Z. Quan, C. Li, Z. Hou, W. Wang and J. Lin, *J. Solid State Chem.* **2009**, *182*, 1045-1054.

[2] a) W. N. Sawka, J. F. Banfield and B. W. Chappell, *Geochim. Cosmochim. Acta* **1986**, *50*, 171-175; b) A. Kumari, R. Panda, M. K. Jha, J. Y. Lee, J. R. Kumar and V. Kumar, *J. Ind. Eng. Chem.* **2015**, *21*, 696-703.

[3] a) H. Onoda, H. Nariai, A. Moriwaki, H. Maki and I. Motooka, *J. Mater. Chem.* **2002**, *12*, 1754-1760; b) K. Ramesh, Y. L. E. Goh, C. Gwie, C. Jie, T. J. White and A. Borgna, *J. Porous Mater.* **2012**, *19*, 423-431.

[4] T. R. Goodman and M. Amurao, *Radiographics* **2012**, *32*, 1829-1837.

[5] F. X. Zhang, J. W. Wang, M. Lang, J. M. Zhang, R. C. Ewing and L. A. Boatner, *Phys. Rev. B* **2009**, *80*, 184114.

[6] Y. Ni, J. M. Hughes and A. N. Mariano, *Am. Mineral.* **1995**, *80*, 21-26.

[7] R. S. Hay, E. E. Boakye, P. Mogilevsky, G. E. Fair, T. A. Parthasarathy and J. E. Davis, *J. Am. Ceram. Soc.* **2013**, *96*, 1586-1595.

[8] J. M. Heuser, R. I. Palomares, J. D. Bauer, M. J. L. Rodriguez, J. Cooper, M. Lang, A. C. Scheinost, H. Schlenz, B. Winkler, D. Bosbach, S. Neumeier and G. Deissmann, *J. Eur. Ceram. Soc.* **2018**.

[9] a) N. Huittinen, Y. Arinicheva, P. M. Kowalski, V. L. Vinograd, S. Neumeier and D. Bosbach, *J. Nucl. Mater.* **2017**, *486*, 148-157; b) O. Terra, N. Clavier, N. Dacheux and R. Podor, *New J. Chem.* **2003**, *27*, 957-967.

[10] E. H. Oelkers and J.-M. Montel, *Elements* **2008**, *4*, 113-113.

[11] R. C. Ewing, *Am. Mineral.* **1975**, *60*, 728-733.

[12] a) L. A. Boatner, *Rev. Mineral. Geochem.* **2002**, *48*, 87-121; b) Y. Arinicheva, K. Popa, A. C. Scheinost, A. Rossberg, O. Dieste-Blanco, P. Raison, A. Cambriani, J. Somers, D. Bosbach and S. Neumeier, *J. Nucl. Mater.* **2017**, *493*, 404-411.

[13] A. Meldrum, L. A. Boatner, W. J. Weber and R. C. Ewing, *Geochim. Cosmochim. Acta* **1998**, *62*, 2509-2520.

[14] a) D. Errandonea, A. Muñoz, P. Rodríguez-Hernández, J. E. Proctor, F. Sapiña and M. Bettinelli, *Inorg. Chem.* **2015**, *54*, 7524-7535; b) Y. Teng, X. Wang, Y. Huang, L. Wu and P. Zeng, *Ceram. Int.* **2015**, *41*, 10057-10062; c) S. Neumeier, Y. Arinicheva, Y. Ji, J. M. Heuser, P. M. Kowalski, P. Kegler, H. Schlenz, D. Bosbach and G. Deissmann, *Radiochim. Acta* **2017**, *105*, 961-984.

[15] N. Clavier, N. Dacheux and R. Podor, *Inorg. Chem.* **2006**, *45*, 220-229.

[16] J.-M. Montel, D. Razafimahatratra, B. Ralison, P. De Parseval, M. Thibault and R. Randranja, *Eur. J. Mineral.* **2011**, *23*, 745-757.

[17] N. Dacheux, N. Clavier and R. Podor, *Am. Mineral* **2013**, *98*, 833-847.

[18] W. J. Manthey, *Phys. Rev. B* **1973**, *8*, 4086-4098.

[19] L. D. Carlos and A. L. L. Videira, *Phys. Rev. B* **1994**, *49*, 11721-11728.

[20] K. Binnemans, *Coordination Chemistry Reviews* **2015**, *295*, 1-45.

[21] J. Dexpert-Ghys, M. Faucher and P. Caro, *Phys. Rev. B* **1981**, *23*, 607-617.

[22] G. M. Sheldrick, *Acta Crystallogr., Sect. C* **2015**, *71*, 3-8.

[23] S. E. Hellebrandt, S. Hofmann, N. Jordan, A. Barkleit and M. Schmidt, *Sci Rep.* **2016**, *6*, 33137---33137.

[24] N. Huittinen, Y. Arinicheva, M. Schmidt, S. Neumeier and T. Stumpf, *J. Colloid Interface Sci.* **2016**, *483*, 139-145.

[25] a) R. S. Feigelson, *J. Am. Ceram. Soc.* **1964**, *47*, 257-258; b) Z. De-gao, T. Bing, C. Li-feng, C. Wang, H. Lin-xiang, L. Jian-hong, Z. Shi-ming and L. Yu-yi, *Cryst. Res. Technol.* **2013**, *48*, 369-373.

[26] a) K. Wang, J. Zhang, J. Wang, C. Fang, W. Yu, X. Zhao and H. Xu, *J. Appl. Crystallogr.* **2005**, *38*, 675-677; b) S. Sadhasivam and N. P. Rajesh, *Mater. Res. Bull.* **2016**, *74*, 117-123.

[27] D. J. Cherniak, J. Pyle and R. John, *Am. Mineral.* **2015**, *89*, 1533---1533.

[28] B. Xiao and M. Schmidt, *Inorg. Chem.* **2017**, *56*, 14948-14959.

[29] M. Albin and W. D. Horrocks Jr, *Inorg. Chem.* **1985**, *24*, 895-900.

[30] M. Schmidt, S. Heck, D. Bosbach, S. Ganschow, C. Walther and T. Stumpf, *Dalton Trans.* **2013**, *42*, 8387-8393.

[31] G. Chen, R. G. Haire and J. R. Peterson, *Appl. Spectrosc.* **1992**, *46*, 273-276.

[32] K. A. Gschneidner, *Handbook on the Physics and Chemistry of Rare Earths, volume 23*, Elsevier, **1996**.

[33] M. Poloznikova and V. V. Fomichev, *Russ. Chem. Rev.* **1994**, *63*, 399-409.

[34] J. Bruno, D. Bosbach, D. A. Kulik and A. Navrotsky, *Chemical Thermodynamics of Solid Solutions of Interest in Nuclear Waste Management*, OECD Publishing: London (Vol. 10), **2007**.

[35] R. D. Shannon, *Acta Crystallogr., Sect. A: Found. Crystallogr.* **1976**, *32*, 751-767.

[36] Y. Hikichi and T. Nomura, *J. Am. Ceram. Soc.* **1987**, *70*, C252-C253.
[37] a) L. Li, Y. Lin, L. Zhang, Q. Cai and Y. Yu, *Cryst. Growth Des.* **2017**, *17*, 6541-6549; b) L. Li, Y. Yu, G. Wang and L. Zhang, *RSC Advances* **2014**, *4*, 37041-37046.
[38] *International Centre for Diffraction Data—Reference Code, HoPO4(26-0746), YbPO4(45-0530), TmPO4(26-0993), YPO4(11-0254), ErPO4(09-0383), LuPO4(43-0003)*.
[39] G. M. Sheldrick, *Acta Crystallogr., Sect. A* **2008**, *64*, 112-122.
[40] Y. Arinicheva, N. Clavier, S. Neumeier, R. Podor, A. Bukaemskiy, M. Klinkenberg, G. Roth, N. Dacheux and D. Bosbach, *J. Eur. Ceram. Soc.* **2018**, *38*, 227-234.
[41] a) A. Barkleit, H. Foerstendorf, B. Li, A. Rossberg, H. Moll and G. Bernhard, *Dalton Trans.* **2011**, *40*, 9868-9876; b) K. Guckel, S. Tsushima and H. Foerstendorf, *Dalton Trans.* **2013**, *42*, 10172-10178; c) K. Schmeide, S. Gürtler, K. Müller, R. Steudtner, C. Joseph, F. Bok and V. Brendler, *Appl. Geochem.* **2014**, *49*, 116-125.
[42] M. Schmidt, T. Stumpf, M. Marques Fernandes, C. Walther and T. Fanghänel, *Angew. Chem. Int. Ed.* **2008**, *47*, 5846-5850.
[43] K. Binnemans and C. Görller-Walrand, *J. Rare Earth.* **1996**, *14*, 173-180.
[44] E. F. Kaelble, *Handbook of X-Rays*, McGraw-Hill, New York, **1967**.

FULL PAPER

A series of europium-substituted xenotime bulk single crystals, $LnPO_4$ (Ln = Tb, Y, Ho, Er, Yb and Lu), were prepared and systematically characterized by polarization-dependent time resolved laser luminescence spectroscopy (p-TRLFS). The polarized spectra demonstrate dependence of the dopant site symmetry on the difference in the ionic radii of the host cations.

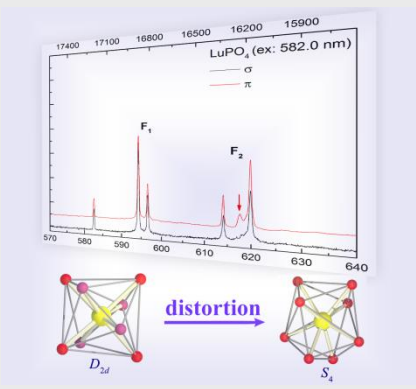

*Bin Xiao, Henry Lösch, Nina Huittinen, and Moritz Schmidt**

Page No. – Page No.

Local structural effects of Eu^{3+} incorporation into xenotime-type solid solutions with different host cations